# The scatter about the 'Universal' dwarf spheroidal mass profile: a kinematic study of the M31 satellites And V and And VI

M. L. M. Collins,[1]* S. C. Chapman,[1] R. M. Rich,[2] M. J. Irwin,[1] J. Peñarrubia,[1] R. A. Ibata,[3] N. Arimoto,[4] A. M. Brooks,[5] A. M. N. Ferguson,[6] G. F. Lewis,[7] A. W. McConnachie[8] and K. Venn[9]

[1]*Institute of Astronomy, Madingley Rise, Cambridge CB3 0HA*
[2]*Department of Physics and Astronomy, University of California, Los Angeles, CA 90095-1547, USA*
[3]*Observatoire de Strasbourg, 11, rue de l'Université, F-67000, Strasbourg, France*
[4]*National Astronomical Observatory of Japan, Osawa 2-21-1, Mitaka, Tokyo, Japan*
[5]*California Institute of Technology, M/C 350-17, Pasadena, CA 91125, USA*
[6]*Institute for Astronomy, University of Edinburgh, Royal Observatory, Blackford Hill, Edinburgh EH9 3HJ*
[7]*Sydney Institute for Astronomy, School of Physics, A29, University of Sydney, NSW 2006, Australia*
[8]*NRC Herzberg Institute for Astrophysics, 5071 West Saanich Road, Victoria, British Columbia, Canada, V9E 2E7*
[9]*Department of Physics and Astronomy, University of Victoria, 3800 Finerty Road, Victoria, BC V8P 1A1, Canada*

## ABSTRACT

While the satellites of the Milky Way (MW) have been shown to be largely consistent in terms of their mass contained within one half-light radius ($M_{half}$) with a 'universal' mass profile, a number of M31 satellites are found to be inconsistent with these relations, and seem kinematically colder in their central regions than their MW cousins. In this work, we present new kinematic and updated structural properties for two M31 dwarf spheroidals (dSph), And V and And VI, using data from the Keck Low Resolution Imaging Spectrograph (LRIS) and the DEep Imaging Multi-Object Spectrograph (DEIMOS) instruments and the Subaru Suprime-Cam imager. We measure systemic velocities of $v_r = -393.1 \pm 4.2$ and $-344.8 \pm 2.5$ km s$^{-1}$, and dispersions of $\sigma_v = 11.5^{+5.3}_{-4.4}$ and $9.4^{+3.2}_{-2.4}$ km s$^{-1}$ for And V and And VI, respectively, meaning these two objects are consistent with the trends in $\sigma_v$ and $r_{half}$ set by their MW counterparts. We also investigate the nature of this scatter about the MW dSph mass profiles for the 'classical' (i.e. $M_V < -8$) MW and M31 dSph. When comparing both the 'classical' MW and M31 dSph to the best-fitting mass profiles in the size–velocity dispersion plane, we find general scatter in both the positive (i.e. hotter) and negative (i.e. colder) directions from these profiles. However, barring one exception (CVnI) only the M31 dSph are found to scatter towards a colder regime, and, excepting the And I dSph, only MW objects scatter to hotter dispersions. The scatter for the combined population is greater than expected from measurement errors alone. We assess this divide in the context of the differing disc-to-halo mass (i.e. stars and baryons to total virial mass) ratios of the two hosts and argue that the underlying mass profiles for dSph differ from galaxy to galaxy, and are modified by the baryonic component of the host.

**Key words:** galaxies: dwarf – galaxies: kinematics and dynamics – Local Group – galaxies: photometry – dark matter.

## 1 INTRODUCTION

The past few years have been a revelation for the kinematic properties of the dwarf spheroidals (dSph) of the Local Group. Strigari

et al. (2008) compiled kinematic data for 18 of the Milky Way dSph galaxies using a maximum likelihood technique based on the Jeans equation to determine the masses for each of these systems within a 300-pc radius ($M_{300}$). This radius was chosen as the masses of these objects are best constrained within the region where there are tracers of the potential (i.e. stars) and for their sample, 300 pc represented the average radius for this region. They determined that despite a

*E-mail: mlmc2@ast.cam.ac.uk

luminous range of more than 4 orders of magnitude, the objects were consistent with having a dynamical mass of $10^7\,M_\odot$ within 300 pc of their centre, and declared this as a common mass scale for dSph galaxies. This characteristic mass scale had already been observed for the brighter dSph ($M_V \leq -8$, Mateo 1998), but the consistency of the fainter objects was a surprise. Further, they showed that the dSph were all consistent in having formed in stellar haloes with total masses $\gtrsim 10^9\,M_\odot$, which could implicate this as the cut-off mass for star formation within cold dark matter haloes, or the minimum mass with which a dark matter halo could form. This work was then extended by Walker et al. (2009) and Wolf et al. (2010), both of whom showed that the Milky Way (MW) dSph haloes exhibit a correlation between global velocity dispersion and half-light radius, and as such, the central densities of their dark matter haloes do not show significant scatter over a large range of luminous scale-radii. Walker et al. (2009) used this observation to postulate that the dSph of MW appear to be consistent with having formed with a 'Universal' dark matter halo mass profile. In addition, follow-up work by Walker et al. (2010) demonstrated that the haloes of these dark matter dominated systems are also consistent with the mean rotation curve derived for spiral galaxies in McGaugh et al. (2007), indicating a constant dark matter central surface density for galaxies ranging from MW dSph to spirals. Recent results presented by both the Pan-Andromeda Archaeological Survey (PAndAS) and the Spectroscopic and Photometric Landscape of Andromeda's Stellar Halo (SPLASH) groups have indicated significant differences between the kinematic temperatures (or velocity dispersions) of the dark matter haloes of dSph orbiting MW versus those orbiting Andromeda, with a number of the latter being seemingly colder for a given half-light radius, and therefore less massive and less dense (Collins et al. 2010; Kalirai et al. 2010), signalling that this Universal mass profile may not extend to dSph found outside of MW. They are also outliers to the McGaugh et al. (2007) rotation curve relations as discussed in Walker et al. (2010). This strongly suggests that while many dSph appear similar in terms of their central densities, they are not all embedded within dark matter haloes that follow a Universal profile.

Interpreting the observed differences in the subhaloes for these two populations is not trivial as it requires an understanding of why some dSph are born, or currently reside in, dark matter haloes with differing physical and dynamical properties. One explanation could be that the physical processes underlying the formation of dSph haloes differ between MW and M31; this clearly conflicts with our current cosmological paradigm for the growth of dark matter haloes. Another possibility is that the M31 subhaloes could have formed later than the MW population when the Universe was less dense, resulting in colder, less dense subhaloes. MW is thought to have had a more quiescent merger history than M31, accreting less baryons over cosmic time. This means that MW could have 'formed' earlier (i.e. reached its half-mass earlier) than M31. It is unclear as to how much later it would need to form to reproduce these results, so more modelling is required to investigate this scenario fully. Finally, recent work by Peñarrubia et al. (2010) put forward a more physically motivated theory for this difference. Using $N$-body simulations, they demonstrated that subhaloes that evolve in host environments with disc-to-halo mass ratios of twice that measured in MW naturally end up with less mass within their half-light radii, very similar to the observations of the M31 population. This fits nicely with the results of Hammer et al. (2007), where they report that M31 has been more successful at accreting baryons than MW, resulting in a stellar population that is ~2.5 times the mass of the MW stellar population.

While there is a tendency for M31 dSph to inhabit colder, lower mass haloes, it is by no means observed throughout the population. Almost half of all spectroscopically surveyed M31 satellites (five out of 12 – And I, And VII, And XIII, And XV and And XVI; Letarte et al. 2009; Collins et al. 2010; Kalirai et al. 2010) have been observed to have velocity dispersions that are entirely consistent with their MW counterparts, suggesting an overall scatter within this population. Therefore, how significant is this subset of kinematically colder M31 dSph? Could this trend be the result of observational biases present in both systems? Due to our position in MW, located within the disc at a distance of 785 kpc from M31, we are obviously not able to observe exactly the same subset of dSph galaxies in our own halo compared to that of M31. In MW, we are hampered by obscuration from components of our own Galaxy that prevent an areal coverage of the system. However, for the region that has been covered in large all-sky surveys (such as SDSS) we are thought to be complete in our detections of bright, 'classical'-type dSph. (Koposov et al. 2008; Tollerud et al. 2008). In M31 the limiting factors in dwarf detection are attributed to the large distance between ourselves and our neighbour, which prevents us from observing objects with $M_V > -6$. We also struggle to identify dwarf galaxies that lie close to the centre of M31 (at $R_{M31} < 40$ kpc) as these objects are obscured (either directly or via projection effects) by the large disc component of the galaxy (traced out as far as 40 kpc kinematically and 25–30 kpc photometrically). We also observe more bright dSph at large distances from the centre of M31 than we do in MW, resulting in a mean distance of satellite from host of 184 kpc in M31 compared with 138 kpc in MW (McConnachie et al. 2009; Richardson et al. 2011).

The study of the intrinsic properties of dSph has also been illuminated by the surprising behaviour that has been observed in some of the least luminous members of this population, the 'ultrafaint' dSph. Since 2005, a large number of very faint objects ($-2 > M_V > -7$, e.g. Willman et al. 2005b; Belokurov et al. 2006, 2007; Zucker et al. 2006b,a; Belokurov et al. 2008) have been discovered, and have revealed several unusual properties for the population. For example, they appear to be hugely dark matter dominated, resulting in a significant departure from the well-established mass–luminosity relationship for such objects (Mateo 1998). The exact morphological nature of these objects is also a subject of some controversy as they possess properties that are common to both dSph and globular clusters and are therefore difficult to classify as either, such as the unusual objects, Willman 1 and Segue 1 (Willman et al. 2005a; Belokurov et al. 2007; Niederste-Ostholt et al. 2009; Simon et al. 2010; Willman et al. 2010). They may also be far from dynamical equilibrium, and instead are undergoing extreme tidal disruption, inflating their observed velocity dispersions and inferred mass-to-light ratios (e.g. Segue 1 and Hercules, Niederste-Ostholt et al. 2009; Sand et al. 2009; Jin & Martin 2010), resulting in a misleading representation of the behaviour of these low-luminosity satellites. These faint objects are observed within a regime where inflation of the velocity dispersion from binary star systems is non-negligible (McConnachie & Côté 2010; Minor et al. 2010), meaning that their dynamical dispersions may be lower than the values quoted in the literature, drastically altering the inferred $M/L$ ratios. Therefore, if we restrict ourselves to comparing solely the dSph whose kinematic properties are free from such uncertainties for the two host galaxies, does this variation persist? And what of its significance?

To answer these questions, we have embarked upon a limited comparison of 'classical' M31 and MW dSph, where we define 'classical' to be any object with $M_V < -7.9$, with particular focus

on two M31 dSph that have recently been spectroscopically observed, And V and And VI, allowing us to present their kinematic properties for the first time. As And V and And VI represent the last two classical dSph that belong to either MW or M31 to have their velocity dispersions and masses measured, these observations make for a timely consideration of the whole ensemble of classical dSph.

## 2 OBSERVATIONS AND ANALYSIS TECHNIQUES

### 2.1 And V

#### 2.1.1 Structural properties with Subaru Suprime-Cam

Andromeda V is a bright M31 satellite with $M_V = -9.8$ (McConnachie & Irwin 2006a), and was first discovered with the Second Palomar Sky Survey (Armandroff, Davies & Jacoby 1998). Its detailed structural properties were assessed using Isaac Newton Telescope (INT) data by McConnachie & Irwin (2006a). This imaging was performed in Johnson $V$ and Gunn $i$ band with the Wide Field Camera (WFC), and was deep enough to observe the top few magnitudes of the red giant branch (RGB) for this object allowing the measurement of the surface brightness profile, intensity-weighted centre, position angle, ellipticity and scale-radii of the dSph using resolved counts of RGB stars. We summarize their results in Table 1. During the nights of 2005 August 3–5, deep Subaru Suprime-Cam imaging of a number of Andromeda dSph, including And V were obtained (PI N. Arimoto) in the Cousins $V$ and $I_c$ bands. Conditions were photometric throughout with typical seeing of 0.5 arcsec. Full details regarding the observing strategy and reduction techniques for this survey are outlined in McConnachie, Arimoto & Irwin (2007), but we briefly summarize here. Objects were typically observed in $5 \times 440$ and $20 \times 240$ s exposures in $V$ and $I_c$ bands, respectively, allowing equivalent depths to be reached in both the bands. Data were processed using the CASU photometric pipeline Irwin & Lewis (2001), which debiased, flat-fielded, trimmed and gain corrected the images. Then, a catalogue was generated for each image frame, morphologically classifying each object as stellar, non-stellar and noise-like. We show in Fig. 1 the colour–magnitude diagram (CMD) generated from the stellar-classified objects from these observations, where we have corrected for extinction and reddening using the maps of

**Table 1.** Structural properties of And V derived in McConnachie & Irwin (2006a) and in this work.

| Property | M06a | This work |
|---|---|---|
| $\alpha_0$ (h:m:s) | 01:10:17.0 | 01:10:17.9 |
| $\delta_0$ (°:′:″) | +47:37:46 | +47:37:38.0 |
| $\theta$ (°) | 32 ± 3 | 32 ± 2 |
| $\epsilon$ | 0.18 ± 0.03 | 0.17 ± 0.02 |
| $r_e$ (arcmin) | 0.86 ± 0.05 | 0.88 ± 0.09 |
| $r_p$ (arcmin) | 1.56 ± 0.08 | 1.59 ± 0.1 |
| $r_c$ (arcmin) | 1.2 ± 0.2 | 1.2 ± 0.1 |
| $r_t$ (arcmin) | 5.3 ± 0.4 | 5.4 ± 0.8 |
| $r_t$ (kpc) | 1.2 ± 0.2 | 1.2 ± 0.2 |
| $r_{half}$ (arcmin) | 1.3 | 1.3 ± 0.1 |
| $r_{half}$ (pc) | 300 | 292 ± 22 |
| $[Fe/H]^a_{phot}$ | −1.6 | −1.6 ± 0.3 |

$^a$Error represents dispersion.

Schlegel, Finkbeiner & Davis (1998). We now use this data set to revise the structural properties of And V. To do this, we follow the same star count method detailed in McConnachie & Irwin (2006b) so that we can make a like-for-like comparison of the Subaru and INT data. Briefly, we construct an isopleth map of a $60 \times 60$ arcmin$^2$ field from the Subaru data centred on And V, then determine the centre of gravity, $\alpha_0$, $\delta_0$; position angle $\theta = 32° \pm 2°$ (measured from east to north); and ellipticity, $\epsilon = 0.17 \pm 0.02$, for each isophote by using the intensity-weighted moments and McConnachie & Irwin (2006b) equations (2) and (3). We then construct a background-corrected radial profile for And V, where a background level is estimated by measuring the average number of stars per arcmin within circular annuli located beyond the tidal radius of And V (as derived in McConnachie & Irwin 2006a). We then subtract this average background from star counts performed in elliptical annuli based on the centre of the dSph, and fit the resulting profile with exponential, Plummer and King profiles. Both the radial profile and best-fitting models are displayed in Fig. 2. From this, we estimate the half-light radius (using our result for the exponential scale-radius, $r_e = 0.88$ arcmin) to be $r_{half} = 1.3$ arcmin and (for the King model) tidal radius of $r_t = 5.4$ arcmin. Using the distance modulus of 24.44 (774 kpc, McConnachie et al. 2005) this gives $r_{half} = 292 \pm 22$ pc and $r_t = 1.2 \pm 0.1$ kpc. Our results are also summarized in Table 1.

We inspected the photometric metallicities of the And V stars using the Dartmouth isochrone models (Dotter et al. 2008). We select an age of 10 Gyr and $[\alpha/Fe] = +0.2$ as numerous studies of dwarf spheroidals have shown them to be composed of old stellar populations that are enhanced in $\alpha$-elements. We interpolate between these isochrones on a fine grid, and present the resulting metallicity distribution function (MDF) in Fig. 3. We find a mean metallicity of $[Fe/H] = -1.6$ for the And V members and a dispersion of 0.3 dex. However, as our imaging is not deep enough to realize the main-sequence turn-off (MSTO) of And V, we cannot reliably ascertain the precise ages and $\alpha$-abundances of the stellar populations. The effect of increasing (decreasing) the age used for our isochrones by $\sim 2$ Gyr results in a shift of $-0.1$ ($+0.1$) dex to our mean metallicities. Similarly, and increase (decrease) in our assumed value of $[\alpha/Fe]$ by 0.2 dex shifts our mean metallicity by $-0.1$ ($+0.1$) dex. This results in a combined uncertainty of $\pm 0.2$ dex.

#### 2.1.2 Kinematic properties with Keck I LRIS

And V was observed using the Low Resolution Imaging Spectrograph (LRIS), situated on the Cassegrain focus of the Keck I telescope on Mauna Kea, on 2009 August 16. The 831/8200 grating was employed with the $I$-band filter on the LRIS Red II detector system, giving a resolution of $\sim 3.0$ Å ($R \sim 2800$). Our observations were taken in an average of 0.7 arcsec seeing, covering a wavelength range of 6900–9000 Å, in the region of the calcium triplet (Ca II). We took $4 \times 15$ min exposure, which resulted in typical signal-to-noise ratios of S:N = 3–10 Å$^{-1}$. Targets were selected using the Subaru CMD shown in Fig. 1, prioritizing stars with $20.3 < i < 23.0$ from within the locus of the clearly defined RGB. In total, we observed 45 science targets within the And V mask, 38 of which reduce successfully.

To reduce the LRIS data, we used the IRAF NOAO.TWODSPEC and NOAO.ONEDSPEC packages. The spectra were flat-fielded, debiased and wavelength calibrated, as well as cleaned of skylines and cosmic rays. We then performed heliocentric velocity corrections to each of our observed stars. Our velocities and errors were derived
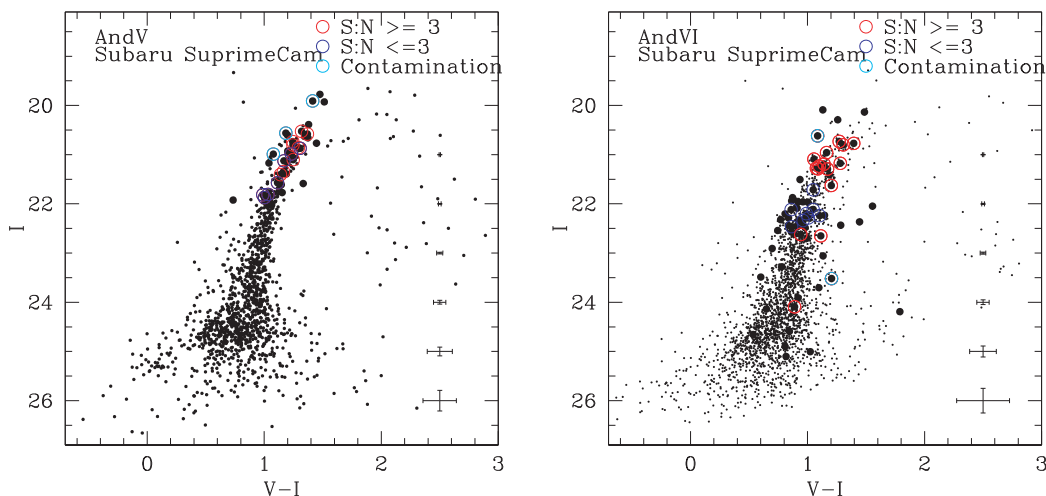
**Figure 1.** Extinction-corrected CMDs of And V and And VI (Subaru, *V* and *I$_c$*) for all stellar objects within $1 \times r_{\mathrm{half}}$ of the dSph centres (small black points). In both cases, the RGB is clearly seen. Red circles indicate confirmed spectroscopic members for each dSph with S:N>3, blue circles indicate confirmed spectroscopic members for each dSph with S:N<3 and cyan circles indicate stars with velocities that are consistent with the dSph systemic velocity, but are potential M31 halo contaminants. Larger black points indicate stars that were observed spectroscopically, but whose velocities are inconsistent with the systemic velocities for And V and And VI. Error bars show the average 1$\sigma$ uncertainties in the photometry at each magnitude level.
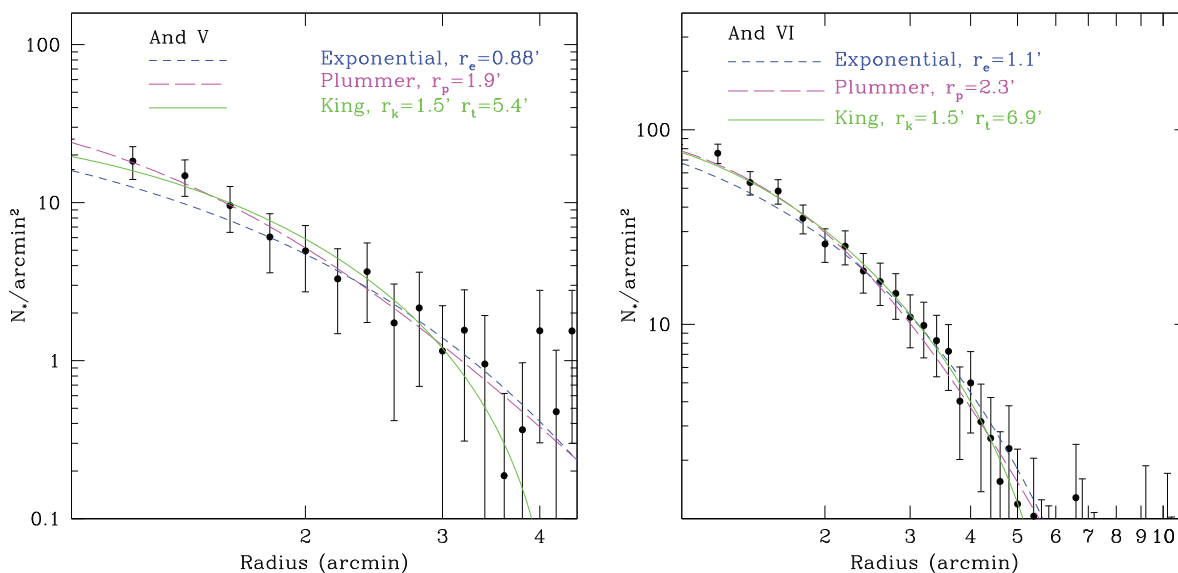


**Figure 2.** Radial profile for And V (left) and And VI (right) constructed from aperture star counts in the region of both dSph. In each case, an average background number density was estimated from an annulus located between 8 and 12 arcmin from the centre of each object, and the results were subtracted from our star counts. We overlay the best-fitting Exponential (blue short dashed line), Plummer (magenta long-dash line) and King (green solid line) profiles in each case also.

from the Ca II triplet lines located at ∼8500 Å, using the same technique described in Collins et al. (2010). Briefly, we used an error-weighted cross-correlation technique with a model template of the Ca II feature at the rest-frame wavelength positions of the triplet lines. We repeated the cross-correlation 1000 times, adding random Poisson noise to our spectra on each occasion, and took the average and standard deviations of these as our velocities and associated errors. We then combine these errors with ones derived by performing separate cross-correlations to each of the Ca II lines in turn, using the dispersion of the resulting velocities. This results in typical errors of 5–15 km s$^{-1}$, with a mean for our sample of 6.8 km s$^{-1}$.

## 2.2 And VI

### 2.2.1 Structural properties with Subaru Suprime-Cam

And VI is one of the more luminous of the M31 classical dSph, with $M_V = -11.5$ (McConnachie & Irwin 2006a), and it too was discovered using the Second Palomar Sky Survey (Armandroff, Jacoby & Davies 1999). Its structural properties were assessed from INT WFC photometry by McConnachie & Irwin (2006b) in the same manner as And V. These results are summarized in Table 2. And VI was also observed in our Subaru Suprime-Cam survey, and the data were taken and reduced in the same way as described
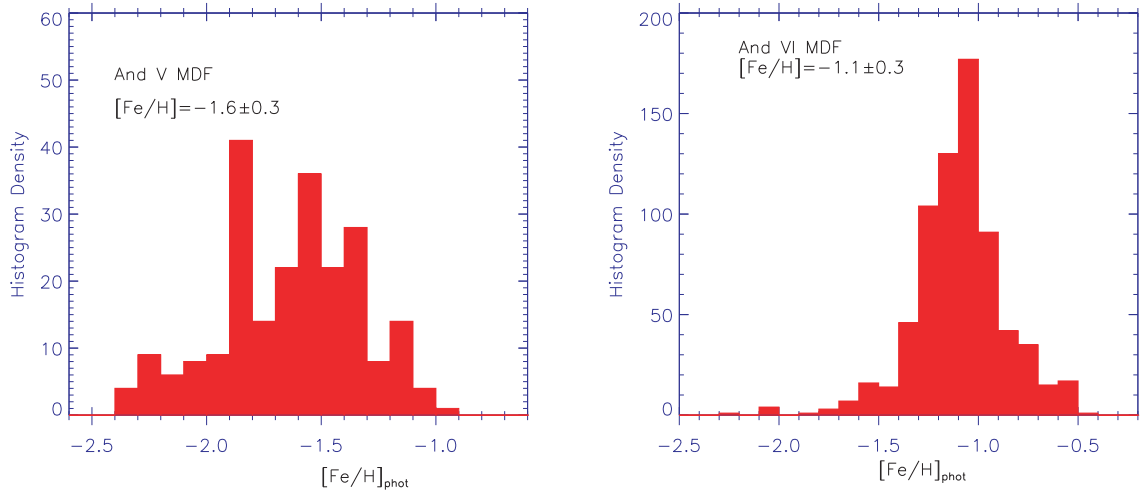
**Figure 3.** The MDF for And V and And VI, constructed from metallicities for stars within $2r_{half}$ of the centre of each dSph. These were calculated by interpolating between a fine grid of Dartmouth isochrones (Dotter et al. 2008) with $[\alpha/Fe] = +0.2$ and an age of 10 Gyr. The mean metallicity is found to be $[Fe/H] = -1.6 \pm 0.3$ and $-1.1 \pm 0.3$ dex for And V and And VI, respectively, where the error represents the dispersion of the population.

**Table 2.** Structural properties of And VI derived in McConnachie & Irwin (2006a) and in this work.

| Property | M06a | This work |
|---|---|---|
| $\alpha_0$ (h:m:s) | 23:51:46.9 | 23:51:47.3 |
| $\delta_0$ (°:′:″) | +24:34:57 | +24:34:52.5 |
| $\theta$ (°) | $163 \pm 3$ | $164 \pm 2$ |
| $\eta$ | $0.41 \pm 0.03$ | $0.39 \pm 0.02$ |
| $r_e$ (arcmin) | $1.2 \pm 0.04$ | $1.1 \pm 0.04$ |
| $r_p$ (arcmin) | $2.15 \pm 0.08$ | $2.3 \pm 0.08$ |
| $r_c$ (arcmin) | $2.1 \pm 0.2$ | $1.5 \pm 0.1$ |
| $r_t$ (arcmin) | $6.2 \pm 0.4$ | $7.0 \pm 0.8$ |
| $r_t$ (kpc) | $1.4 \pm 0.1$ | $1.6 \pm 0.2$ |
| $r_{half}$ (arcmin) | 1.8 | $1.9 \pm 0.07$ |
| $r_{half}$ (pc) | 420 | $440 \pm 16$ |
| $[Fe/H]_{phot}^a$ | $-1.3$ | $-1.1 \pm 0.3$ |

$^a$Error represents dispersion.

above. We display the CMD of stellar objects from these data within $1 \times r_{half}$ of And VI in Fig. 1. The data start to become incomplete at an S:N of 10, which corresponds to $V = I \sim 25.5$.

In this section, we rederive the structural parameters for And VI, using these Subaru data and the same approach as detailed for And V. Again, from the star counts and isopleths maps we find a good agreement with those of the INT study. Our results are summarized in Table 2. We calculate $r_{half} = 1.9$ arcmin (from our exponential scale-radius), $r_t = 7.0$ arcmin, $\epsilon = 0.39$ and $\theta = 164°$. Using the McConnachie et al. (2005) distance for And VI of 783 kpc (distance modulus of 24.47) we obtain the physical scale-radii of $r_{half} = 440 \pm 16$ pc and $r_t = 1.6 \pm 0.2$ kpc.

We perform the same isochrone analysis for And VI as that described in Section 2.1.1, and the resulting MDF is displayed in Fig. 3. The same difficulties in ascertaining robust photometric metallicities for And V are experienced here, as the Subaru data do not reach the MSTO. We find a median metallicity of $[Fe/H] = -1.1 \pm 0.3$, where the error represents the dispersion of the population. This dispersion is the same as we measure for And V, despite And VI having a much broader RGB. And V is more metal poor than And VI with an average metallicity of $[Fe/H] = -1.6$. As you decrease

in metallicity, isochrones for a given age and $\alpha$-abundance begin to bunch together in colour space $(V - I)$, meaning smaller differences in colour translate to larger differential metallicities, driving a larger metallicity dispersion for a smaller colour range.

### 2.2.2 Kinematic properties with Keck II DEIMOS

The DEep-Imaging Multi-Object Spectrograph (DEIMOS), situated on the Nasmyth focus of the Keck II telescope is an ideal instrument for obtaining medium-resolution ($R \sim 6000$) spectra of multiple, faint stellar targets in the M31 dSph. The data for And VI were taken on the nights of 2009 September 17–19 in photometric conditions and with <1 arcsec seeing. Our chosen instrumental setting covered a wavelength range of 5600–9800 Å and for our exposures we implemented $3 \times 30$ min integrations, and employed the 1200 line mm$^{-1}$ grating, giving us a spectral resolution of $\sim$1.37 Å. The spectra from this set-up typically possess S:N of $>3$ Å$^{-1}$. Due to the position of And VI in the sky, this object was observed at the beginning of each night meaning that it suffered from a high airmass of 2.2, so the S:N for these stars are lower than expected for comparable length exposures taken at a lower airmass. The typical errors within the mask range from 5–12 km s$^{-1}$, with a mean for our sample of 6.2 km s$^{-1}$.

### 2.3 Determining membership

Before we can analyse the kinematic properties of these objects, it is important to correctly determine the bona fide members of the dSph, and to eliminate stars which belong to the MW foreground (mostly $v_r > -160$ km s$^{-1}$) or the M31 halo ($v_r \sim -300$ km s$^{-1}$). As both And V and And VI lie at a large projected radius from the centre of M31 ($\sim$110 and 270 kpc, respectively, Armandroff et al. 1998, 1999), the density of stars, and thus the number of contaminants, belonging to the M31 halo should be very low for these objects, but should still be considered. As And V is located at a higher latitude than And VI, this dwarf is more likely to experience contamination from MW, and so this must be treated carefully. In order to minimize the contamination to our sample, we require the following conditions to be met by bona fide members.

(i) Stars must fall on the RGB of dSph, as defined by colour cuts in *V* and *I* bands for And V and And VI.

(ii) Stars must sit within $2r_{half}$ of the dSph centre. Stars at larger radii that satisfy all other criteria barring this are classified as 'tentative members', and their properties and probabilities of being members will be discussed.

(iii) Stars must show low Na I doublet absorptions (i.e. equivalent width, $EW_{Na I} < 1.4$). Strong Na I absorption may indicate that the observed star is a foreground dwarf star, not an M31 RGB star.

(iv) After deriving a systemic velocity, any star within the sample with a velocity that is $>3\sigma$ from the systemic will not be considered a member. The kinematic properties of the dSph will then be rederived iteratively in this manner until only stars with velocities within $3\sigma$ of the derived systemic velocity remain.

## 3 THE KINEMATICS OF AND V AND VI

### 3.1 Systemic velocities and velocity dispersions

Using the criterion laid out in Section 2.3 we identify the most probable member stars for each of the dSph observed with LRIS and DEIMOS. In Fig. 4 we display the kinematic properties of all the stars observed in each slit mask. The top panel in each case shows a histogram of the velocities of observed stars. The heavy red histogram highlights the kinematic location of each dSph, which is immediately obvious as cold overdensities of stars in velocity space. The central panel shows velocity versus distance from the dwarf centre, where the 1, 2, 3 and 4 × $r_{half}$ are marked as dashed lines. The lower panel shows the velocity as a function of photometric metallicity. Not all stars within the mask have photometric metallicities as their colours place them outside the parameter space covered by our chosen isochrones. Such dropouts are likely Galactic contaminants and not true M31 RGB stars. Cutting on velocity, distance, Na I absorption and metallicity (proxy for position on RGB), we identify 14 and 26 secure members per dSph for And V and And VI, respectively, as well as two and seven (four of which have S:N>3) tentative members beyond 2 × $r_{half}$ that fall within the cold peak, although we treat these cautiously as at the systemic velocities for these objects (~−400 and ~−350 km s$^{-1}$) they fall within

the regime of the M31 halo. In the case of And V, two stars found within the velocity peak do not fall on the RGB of the dwarf (shown as cyan points in Fig. 1), seemingly more metal poor than the And V population, making them likely halo interlopers. For And VI we also identify two outliers from the CMD which again are likely halo contaminants. In both cases, the outliers show no significant Na I absorption, strengthening our assumption that these are M31 halo RGB stars, rather than Galactic halo dwarfs. We show the kinematic properties of all confirmed and tentative members, as well as halo contaminants for And V and And VI in Tables 3 and 4, respectively.

With secure candidates in hand, we now determine the systemic velocities ($v_r$) and velocity dispersions ($\sigma_v$) for each dSph using the maximum likelihood approach of Martin et al. (2007). This is the same technique as we have used in our previous work (e.g. Chapman et al. 2006; Letarte et al. 2009; Collins et al. 2010), and as we briefly summarize here. We calculate $v_r$ and $\sigma$ by sampling a coarse grid in ($v_r$, $\sigma$) space and determining the parameter values that maximize the likelihood function (ML), defined as

$$ML(v_r, \sigma) = \prod_{i=1}^{N} \frac{1}{\sigma_{tot}} \exp\left[ -\frac{1}{2}\left(\frac{v_r - v_{r,i}}{\sigma_{tot}}\right)^2 \right], \qquad (1)$$

where $N$ is the number of stars in the sample, $v_{r,i}$ is the radial velocity measured for the $i$th secure member star, $v_{err,i}$ is the corresponding uncertainty and $\sigma_{tot} = \sqrt{\sigma^2 + v_{err,i}^2}$. In this way, we are able to separate the intrinsic dispersion of the dSph from the dispersion introduced by our measurement uncertainties. We display the one-dimensional likelihood distributions for $v_r$ and $\sigma_v$ in Fig. 5 where the dashed lines represent the conventional $1\sigma$, $2\sigma$ and $3\sigma$ (68, 95 and 99.7 per cent) uncertainties on the values. In the case of the And VI data, we have only included the 12 member stars with S:N > 3 Å in this analysis to avoid introducing large uncertainties into their calculated properties. We determine systemic velocities of $v_r = -393.1 \pm 4.2$ and $-344.8 \pm 3.4$ km s$^{-1}$ and velocity dispersions of $\sigma_v = 11.5^{+5.3}_{-4.4}$ and $9.4^{+3.2}_{-2.4}$ km s$^{-1}$ for And V and VI, respectively. The velocities of these two galaxies (but not dispersions) were previously reported in Guhathakurta, Reitzel & Grebel (2000) to be $v_r = -387.0 \pm 4.0$ and $-340.7 \pm 2.9$ km s$^{-1}$, which agree with our findings within the associated $1\sigma$ errors. We summarize our results in Table 5.
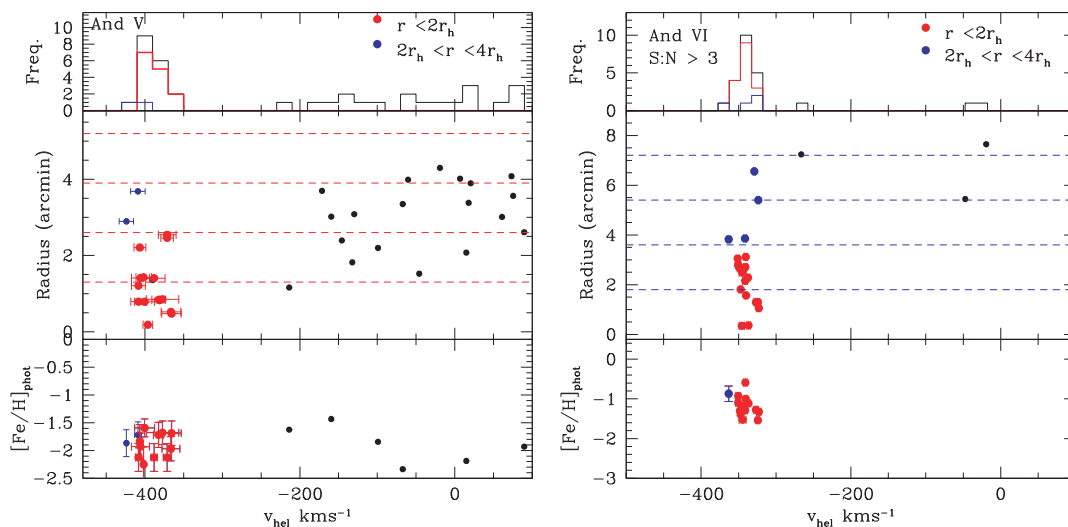


**Figure 4.** The velocities, distances from centre and photometric metallicities of all stars within the LRIS and DEIMOS fields. Some stars do not have photometric metallicities as their colours place them outside the range of isochrones used. Red points indicate likely dSph members and the red dashed lines represent 1, 2, 3 and 4 times the $r_h$ of each dSph. And V and And VI appear as cold overdensities of stars at ~−400 and ~−350 km s$^{-1}$, respectively.

**Table 3.** Kinematic properties of the observed members of And V.

| $\alpha_{2000}$(hh:mm:ss) | $\delta_{2000}$ | $V$ | $I$ | $v_r$ (km s$^{-1}$) | S:N (Å$^{-1}$) | [Fe/H]$_{phot}^a$ | [Fe/H]$_{spec}$ |
|---|---|---|---|---|---|---|---|
| | | | | Confirmed members | | | |
| 1:10:18.62 | 47°38′9″.4 | 22.544 | 21.405 | $-365.6 \pm 12.6$ | 6.5 | $-1.65$ | $-2.1 \pm 0.3$ |
| 1:10:12.19 | 47°37′30″.6 | 21.95 | 20.581 | $-377.3 \pm 21$ | 5.1 | $-1.55$ | $-1.3 \pm 0.3$ |
| 1:10:20.65 | 47°38′15″.7 | 21.979 | 20.735 | $-408.2 \pm 4$ | 4.6 | $-1.85$ | $-2.2 \pm 0.4$ |
| 1:10:20.03 | 47°37′10″.1 | 22.349 | 21.101 | $-400.4 \pm 12.8$ | 4.4 | $-1.48$ | $-1.2 \pm 0.3$ |
| 1:10:16.32 | 47°37′37″.4 | 22.803 | 21.815 | $-396.2 \pm 2.21$ | 4.3 | $-2.15$ | $-1.6 \pm 0.7$ |
| 1:10:22.22 | 47°38′52″.1 | 22.685 | 21.571 | $-405.7 \pm 11.5$ | 4.2 | $-1.55$ | $-2.1 \pm 0.3$ |
| 1:10:25.14 | 47°38′9″.8 | 22.875 | 21.873 | $-401.6 \pm 1.94$ | 3.9 | $-2.05$ | $-2.0 \pm 0.3$ |
| 1:10:17.94 | 47°37′16″.2 | 22.05 | 20.804 | $-366.4 \pm 11.7$ | 3.5 | $-1.78$ | $-1.0 \pm 0.4$ |
| 1:10:06.71 | 47°35′26″.9 | 22.218 | 20.986 | $-423.8 \pm 1.28$ | 3.4 | $-1.65$ | $-1.8 \pm 0.4$ |
| 1:10:09.04 | 47°37′20″.8 | 22.294 | 21.125 | $-388.1 \pm 4.1$ | 3.4 | $-1.78$ | $-1.6 \pm 0.5$ |
| 1:10:24.17 | 47°37′47″.1 | 21.323 | 19.909 | $-408.3 \pm 9.04$ | 2.8 | $-2.12$ | $-1.7 \pm 0.7$ |
| 1:10:21.56 | 47°37′25″.8 | 22.152 | 20.86 | $-382.3 \pm 6.76$ | 2.2 | $-1.55$ | $-1.8 \pm 0.5$ |
| 1:10:05.54 | 47°36′41″.6 | 22.178 | 20.871 | $-406.5 \pm 3.6$ | 2.0 | $-1.48$ | $-1.4 \pm 0.5$ |
| 1:10:02.38 | 47°37′48″.5 | 22.84 | 21.808 | $-371.3 \pm 5.08$ | 1.7 | $-1.85$ | $-2.2 \pm 0.5$ |
| | | | | Tentative members (i.e. stars at $>2 \times r_{half}$) | | | |
| 1:10:07.45 | 47°35′48″.0 | 21.845 | 20.526 | $-371.2 \pm 2.34$ | 3.9 | $-1.9$ | $-1.9 \pm 0.4$ |
| 1:10:38.56 | 47°38′22″.1 | 22.51 | 21.346 | $-409.0 \pm 4.38$ | 3.0 | $-1.55$ | $-2.0 \pm 0.4$ |
| | | | | Outliers | | | |
| 1:10:19.23 | 47°39′4″.1 | 21.748 | 20.563 | $-390.2 \pm 1.32$ | 3.8 | $-2.42$ | $-1.3 \pm 0.5$ |
| 1:10:13.94 | 47°37′9″.0 | 22.067 | 20.989 | $-381.3 \pm 2.03$ | 3.7 | $-2.48$ | $-1.6 \pm 0.7$ |

$^a$Derived from Dotter et al. (2008) isochrones with [$\alpha$/Fe] = +0.2; age is 10 Gyr. Typical errors of ±0.2 dex.

### 3.1.1 Masses and dark matter content

As dSph galaxies are dispersion-supported objects, we can use their internal velocity dispersions to measure a mass for the system, and infer how much dark matter dominated they are. There are several methods in the literature for this (e.g. Illingworth 1976; Richstone & Tremaine 1986); however, these methods make the assumption that mass follows light, something we know to be incorrect from measurements of many dSph systems (e.g. Walker et al. 2007, 2009), whose high masses cannot be explained by the luminous matter only. Recent work by Walker et al. (2009) has shown that the mass contained within the half-light radius ($M_{half}$) of these objects can be reliably estimated using the following formula:

$$M_{half} = \mu r_{half}\sigma_{v,half}^2, \qquad (2)$$

where $\mu = 580\,M_\odot\,$kpc$^{-1}\,$km$^{-1}\,$s$^2$, $r_{half}$ is the half-light radius in kpc and $\sigma_{v,half}$ is the velocity dispersion within the half-light radius. This simple estimator assumes that the stellar component is distributed as a Plummer sphere with an isotropic velocity distribution and a velocity dispersion remains constant throughout the system. If we apply this estimator to And V and And VI, we obtain the following values for $M_{half}$: $2.3^{+1.5}_{-1.3} \times 10^7\,M_\odot$ for And V and $2.1^{+1.0}_{-0.8} \times 10^7\,M_\odot$ for And VI, also summarized in Table 5. From this, it is trivial to estimate the mass-to-light ratios for these objects. The $V$-band luminosities for And V and And VI are $L_V = 5.75 \times 10^6$ and $3.40 \times 10^7\,L_\odot$, and we obtain the following values: $[M/L]_{half} = 78^{+51}_{-44}$ and $12.3^{+5.9}_{-4.7}$ (McConnachie & Irwin 2006a). This demonstrates that each of our objects is likely to be dark matter dominated.-5

### 3.1.2 Metallicities

In Section 2, we used Subaru photometry to measure the photometric metallicities of the RGB stars in And V and And VI. Using Dotter et al. (2008) isochrones with [$\alpha$/Fe] = +0.2 and an age of 10 Gyr, we deduced average metallicities of [Fe/H] = $-1.8$

and $-1.1$ for And V and And VI, respectively. While these values give us a good sense of the relative metallicities of these objects, our photometric data do not go deep enough to realize the MSTO of these dSph, preventing us from deducing accurate ages for the stellar populations within. We are also unable to reliably discern their $\alpha$-abundances, and these factors leave us exposed to the age–[$\alpha$/Fe]–metallicity degeneracy, which attributes an error on our estimates of ±0.2 dex. To gain further insight into the average metallicities of these objects, we can turn to the spectra of the members of each dSph.

As discussed in Section 2, for both And V and And VI, our observational set-up was such that we observed our stars in the wavelength regime of the Ca II triplet. The equivalent widths of this strong absorption feature have been shown by numerous authors (e.g. Battaglia et al. 2008; Starkenburg et al. 2010) to be a very good proxy for the measurement of [Fe/H], down to values as low as [Fe/H] = $-4$ (Starkenburg et al. 2010). Thus, we are able to use this feature to measure the metallicities for the individual stars of And V and And VI as well as for a composite spectrum for each, where we perform an error-weighted co-addition of the spectra of the confirmed members of each satellite. To calculate metallicities from the equivalent widths of the three lines (Ca II$_{8498}$, Ca II$_{8542}$, Ca II$_{8662}$) we use the following relation:

$$[Fe/H] = -2.66 + 0.42[EW - 0.64(V_{HB} - V_{RGB})], \qquad (3)$$

where $EW = 0.5\,$Ca II$_{8498}$+Ca II$_{8542}$+0.6 Ca II$_{8662}$, $V_{HB}$ is the $V$-band magnitude of the horizontal branch (HB) at the distance of M31 (25.17, Harbeck et al. 2005) and $V_{RGB}$ is the $V$-band magnitude of the star (or weighted average $V$-band magnitude of the sample for the composite).

In Fig. 6 we show a number of spectra for our And V and And VI member stars spanning a range of luminosities and S:N, along with their calculated spectroscopic metallicities. When calculating errors we not only include the errors on the fit itself, but systematic errors in measuring the continuum level and the relationship

**Table 4.** Kinematic properties of the observed members of And VI.

| $\alpha_{2000}$(hh:mm:ss) | $\delta_{2000}$ | $V$ | $I$ | $v_r$ (km s$^{-1}$) | S:N (Å$^{-1}$) | [Fe/H]$^a_{\rm phot}$ | [Fe/H]$_{\rm spec}$ |
|---|---|---|---|---|---|---|---|
| | | | | Confirmed members | | | |
| 23:51:44.45 | 24°37′48″.80 | 22.12 | 20.96 | $-347.25 \pm 1.73$ | 5.02 | $-1.22$ | $-2.04 \pm 0.8$ |
| 23:51:50.74 | 24°33′57″.70 | 23.76 | 22.65 | $-340.84 \pm 2.36$ | 4.57 | $-0.70$ | $-0.96 \pm 0.5$ |
| 23:51:45.55 | 24°36′3″.80 | 22.15 | 21.09 | $-324.21 \pm 2.57$ | 4.38 | $-1.35$ | $-0.71 \pm 0.2$ |
| 23:51:52.41 | 24°33′34″.70 | 22.83 | 21.63 | $-340.42 \pm 2.14$ | 4.04 | $-0.80$ | $-1.41 \pm 0.5$ |
| 23:51:51.52 | 24°36′23″.50 | 22.46 | 21.29 | $-345.70 \pm 3.48$ | 3.84 | $-1.04$ | $-0.98 \pm 0.2$ |
| 23:51:46.94 | 24°35′40″.70 | 22.33 | 21.19 | $-326.74 \pm 3.01$ | 3.81 | $-1.12$ | $-1.71 \pm 0.4$ |
| 23:51:48.19 | 24°34′27″.10 | 24.98 | 24.09 | $-337.44 \pm 2.64$ | 3.57 | $-0.92$ | $-1.15 \pm 0.4$ |
| 23:51:41.15 | 24°36′33″.00 | 22.38 | 21.29 | $-341.16 \pm 3.32$ | 3.57 | $-1.15$ | $-0.78 \pm 0.3$ |
| 23:51:46.60 | 24°37′11″.90 | 22.35 | 21.27 | $-323.01 \pm 2.88$ | 3.56 | $-1.18$ | $-2.45 \pm 2.2$ |
| 23:51:50.85 | 24°36′18″.50 | 22.46 | 21.18 | $-336.70 \pm 2.58$ | 3.55 | $-0.99$ | $-1.81 \pm 0.6$ |
| 23:51:44.38 | 24°34′16″.10 | 24.06 | 23.28 | $-350.49 \pm 3.40$ | 3.20 | $-0.73$ | $-0.78 \pm 0.4$ |
| 23:51:46.21 | 24°37′37″.10 | 23.61 | 22.91 | $-347.09 \pm 5.88$ | 3.10 | $-1.18$ | $-1.37 \pm 0.3$ |
| 23:51:46.19 | 24°35′54″.60 | 25.70 | 24.90 | $-332.98 \pm 6.07$ | 2.08 | $-1.15$ | $-1.09 \pm 0.4$ |
| 23:51:41.12 | 24°37′43″.50 | 23.00 | 22.09 | $-308.26 \pm 8.37$ | 2.00 | $-1.05$ | $-1.59 \pm 3.2$ |
| 23:51:54.77 | 24°28′53″.50 | 23.19 | 22.20 | $-339.81 \pm 6.66$ | 1.90 | $-0.80$ | $-1.87 \pm 0.9$ |
| 23:51:46.91 | 24°33′53″.00 | 23.69 | 22.70 | $-314.51 \pm 6.52$ | 1.89 | $-0.95$ | $-0.95 \pm 0.7$ |
| 23:51:54.79 | 24°35′50″.30 | 22.88 | 21.96 | $-328.10 \pm 7.15$ | 1.86 | $-1.10$ | $-1.41 \pm 1.1$ |
| 23:51:44.42 | 24°37′26″.30 | 23.38 | 22.46 | $-348.25 \pm 6.95$ | 1.46 | $-0.83$ | $1.57 \pm 11.1$ |
| 23:51:54.23 | 24°36′42″.80 | 22.80 | 21.94 | $-351.77 \pm 12.16$ | 1.43 | $-1.25$ | $-1.7 \pm 0.9$ |
| 23:51:44.13 | 24°35′45″.10 | 23.37 | 22.44 | $-332.82 \pm 8.19$ | 1.39 | $-0.80$ | $-1.14 \pm 0.6$ |
| 23:51:49.63 | 24°32′42″.20 | 22.98 | 22.12 | $-354.98 \pm 8.92$ | 1.35 | $-1.15$ | $-2.16 \pm 11.4$ |
| 23:51:44.66 | 24°36′37″.90 | 24.83 | 23.91 | $-340.10 \pm 35.83$ | 1.21 | $-1.15$ | $-0.54 \pm 0.5$ |
| 23:51:46.70 | 24°35′16″.50 | 24.09 | 23.49 | $-354.44 \pm 11.69$ | 1.33 | $-1.25$ | $-1.88 \pm 0.7$ |
| 23:51:45.61 | 24°36′47″.10 | 22.92 | 21.96 | $-362.91 \pm 8.38$ | 1.11 | $-1.02$ | $-1.16 \pm 0.9$ |
| 23:51:44.69 | 24°34′42″.30 | 25.44 | 24.59 | $-384.50 \pm 9.38$ | 0.89 | $-0.90$ | $-0.87 \pm 0.9$ |
| 23:51:41.55 | 24°36′28″.10 | 23.27 | 22.44 | $-320.62 \pm 14.57$ | 0.87 | $-1.05$ | $-1.03 \pm 0.9$ |
| | | | | Tentative members (i.e. stars at $>2 \times r_{\rm half}$) | | | |
| 23:51:47.00 | 24°32′56″.00 | 23.56 | 22.62 | $-363.18 \pm 1.85$ | 4.71 | $-0.68$ | $-1.20 \pm 0.3$ |
| 23:51:45.80 | 24°32′31″.20 | 22.76 | 21.71 | $-326.89 \pm 5.04$ | 3.29 | $-1$ | $-1.41 \pm 0.4$ |
| 23:51:54.12 | 24°31′36″.80 | 23.30 | 22.34 | $-348.75 \pm 5.65$ | 3.75 | $-0.78$ | $-1.36 \pm 0.5$ |
| 23:51:49.59 | 24°31′27″.20 | 23.38 | 22.23 | $-345.96 \pm 8.11$ | 3.51 | $-0.57$ | $-1.10 \pm 0.7$ |
| 23:51:49.30 | 24°32′26″.80 | 23.16 | 22.11 | $-343.06 \pm 5.88$ | 1.46 | $-0.74$ | $-2.06 \pm 0.7$ |
| 23:51:45.30 | 24°30′18″.50 | 23.34 | 22.24 | $-351.28 \pm 8.70$ | 1.15 | $-0.60$ | $-1.34 \pm 0.8$ |
| 23:51:47.81 | 24°31′18″.10 | 23.29 | 22.29 | $-320.05 \pm 11.83$ | 1.10 | $-0.73$ | $-1.97 \pm 0.5$ |
| | | | | Outliers | | | |
| 23:51:44.87 | 24°37′31″.90 | 21.70 | 20.62 | $-339.94 \pm 1.55$ | 6.39 | NA | $-1.65 \pm 0.3$ |
| 23:51:44.69 | 24°34′42″.30 | 24.19 | 23.06 | $-384.50 \pm 9.38$ | 0.89 | $-0.20$ | $-1.20 \pm 1.3$ |

$^a$Derived from Dotter et al. (2008) isochrones with $[\alpha/{\rm Fe}] = +0.2$; age is 10 Gyr. Typical errors of $\pm 0.2$ dex.
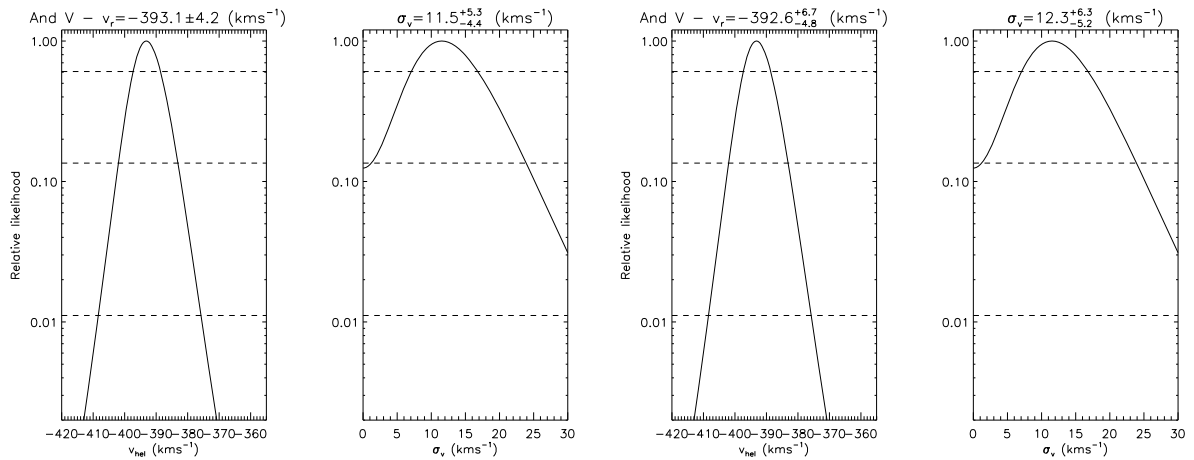


**Figure 5.** ML distributions for the systemic velocities and velocity dispersions of And V (left) and And VI (right). Dashed lines represent the $1\sigma$, $2\sigma$ and $3\sigma$ uncertainties on the peak values. We obtain $v_r = -393.1 \pm 4.2$ and $-344.8 \pm 2.5$ km s$^{-1}$, and $\sigma_v = 11.5^{+5.3}_{-4.4}$ and $9.4^{+3.2}_{-2.4}$ km s$^{-1}$ for And V and And VI, respectively.

**Table 5.** Kinematic properties of And V and And VI.

| Property | And V | And VI |
|---|---|---|
| $v_r$ (km s$^{-1}$) | $-393.1 \pm 4.2$ | $-344.8 \pm 3.4$ |
| $\sigma_v$ (km s$^{-1}$) | $11.5^{+5.3}_{-4.4}$ | $9.4^{+3.2}_{-2.4}$ |
| [Fe/H]$_{\rm spec}$ | $-1.6 \pm 0.3$ | $-1.3 \pm 0.14$ |
| $M_{\rm half}$ (M$_\odot$) | $2.3^{+1.5}_{-1.3} \times 10^7$ | $2.1^{+1.0}_{-0.8} \times 10^7$ |
| $[M/L]_{\rm half}$ | $78^{+51}_{-44}$ | $12.3^{+5.9}_{-4.7}$ |

between the equivalent widths and the measurement of [Fe/H]. As can be seen, for the star-by-star metallicities our [Fe/H] measurements carry significant errors (of order 0.3–0.5 dex or greater), as precision measurements of equivalent widths and the continuum of each star are difficult to accurately assess in this low S:N regime. This inaccuracy can be seen in Tables 3 and 4, where the spectroscopic metallicities are often very different from the photometrically derived metallicities which typically have errors of only ±0.2 dex. From measuring the metallicities of the individual members, we find a range of metallicities for And V from the spectra of [Fe/H] = −2.2 to −1.2, with a mean of [Fe/H] = −1.6. For And VI we find a range of [Fe/H] = −0.9 to −1.8, with a mean of [Fe/H] = −1.4. With the co-added spectra, in Fig. 7, we derive metallicities of [Fe/H] = −1.6 ± 0.3 for And V and [Fe/H] = −1.3 ± 0.14 for And VI. The larger errors on the [Fe/H] for And V are the result of a number of factors. First, we have a lower number of member stars for this dSph, meaning the noise in the resulting spectrum is greater. Second, the spectroscopic resolution of our LRIS set-up is lower than that of our DEIMOS set-up, which can cause broadening effects in the Ca II lines. Finally, as can be seen in both the individual and combined spectra for this object, the third line of the Ca II triplet has been broadened significantly by OH absorption lines in this regime, and so we have excluded this line from our metallicity calculations, using only the first and second lines. This is done with the knowledge that the ratio of equivalent widths of the Ca II lines

when they are not saturated should be 0.4:1:0.75 (Starkenburg et al. 2010), so we can alter the ratios of the Ca II$_{8498}$ lines used in equation (3) from 0.5 to 1.5. We also see broadening in a number of the And VI spectra (as can be seen in Fig. 6), but it is less prevalent throughout the sample. In the case of both And V and And VI, these spectroscopic values agree very well with those we derived from the photometry. They also conform to the observed trend of decreasing metallicity with decreasing luminosity seen in both the MW and M31 dSph populations (Kirby et al. 2008, 2011).

## 4 COMPARING THE 'CLASSICAL' dSph OF M31 AND MW

In the literature, the term 'classical' has been applied to the MW dSph galaxies that were discovered pre–2005 i.e. Carina (Car), Draco (Dra), Fornax (For), Leo I (LeoI), Leo II (LeoII), Sculptor (Scl), and Ursa Minor (UMi). All of these dSph have absolute magnitudes of $M_V \leq -8$. By limiting ourselves to this brighter regime, we can ensure that we have robust estimates for the parameters we are interested in, particularly the velocity dispersions. While there are a few dSph in M31 with $M_V > -8$ that have been spectroscopically surveyed (i.e. And XI, XII and XIII, Chapman et al. 2007; Collins et al. 2010), their RGBs are sparsely populated, leaving us with only a handful of stars (4–8) with which to determine the kinematic properties. This results in large associated errors. For the 'classical' dSph, one is able to obtain velocities for much larger numbers of members, giving us velocity dispersions that are much better constrained. Therefore for the purpose of this study, we require 'classical' dwarfs to be any dSph with $M_V \leq -7.9$. With this luminosity constraint, we ensure a quality control for our M31 dSph, and avoid the regime of the ultrafaints in MW where a number of factors (as discussed in Section 1) make the determination of the masses and velocity dispersions in these systems very difficult. Multiple epoch data are required for these objects in order to constrain their true velocity dispersions (Koposov et al. 2011). We choose a lower cut of
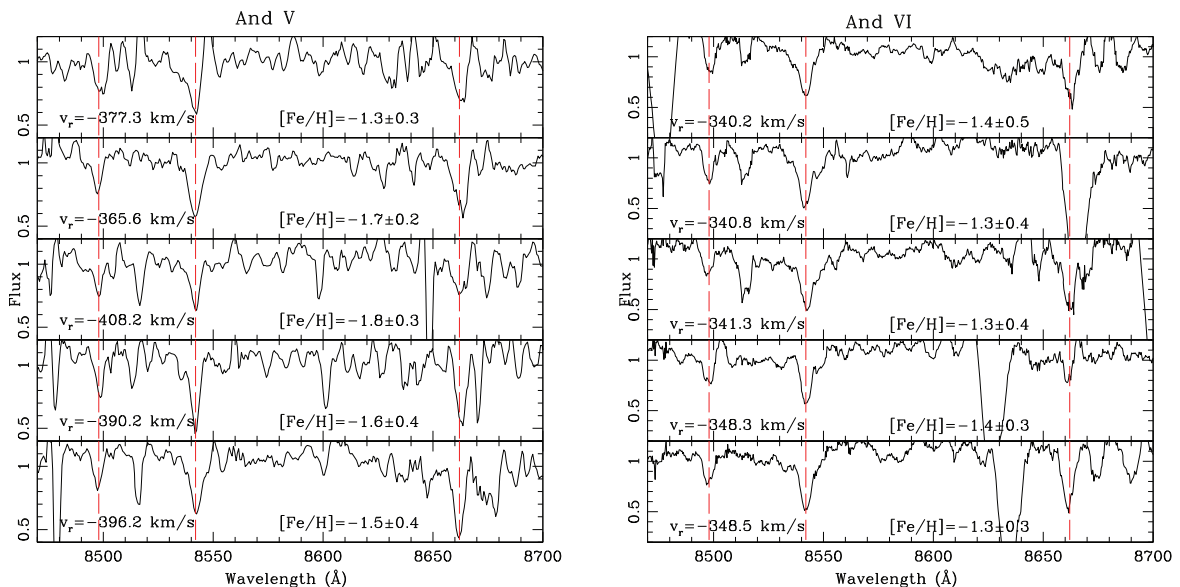
**Figure 6.** Five spectra from individual And V (left) and And VI (right), shifted to the rest-frame and normalized in flux. These span a range of S:N to demonstrate the quality of our data sets. We indicate the positions of the Ca II features with red dashed line. The velocities and spectroscopic metallicities of each star are also shown.
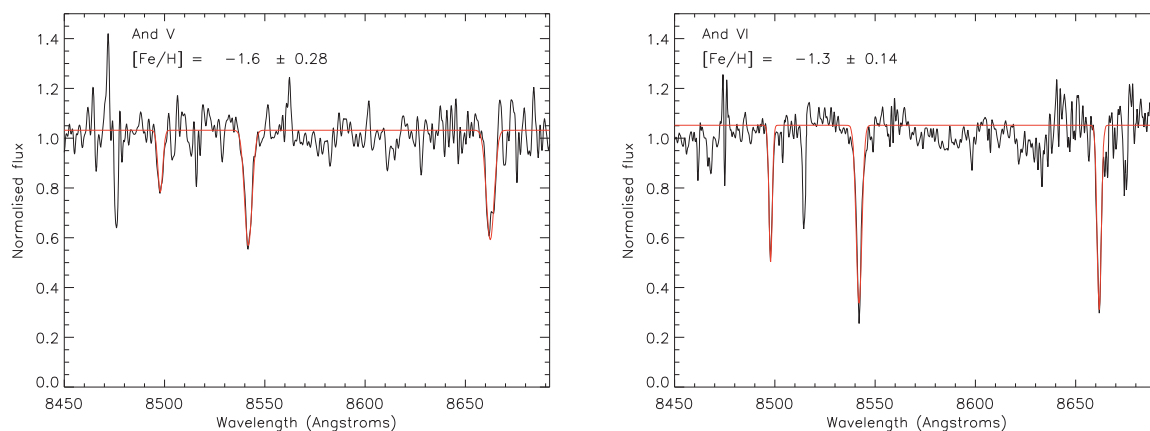
**Figure 7.** Co-added spectra for And V (left) and And VI (right), constructed from member stars of each with S:N>3. We use the Ca II triplet lines to estimate the average metallicity for each dSph and find [Fe/H] = $-1.6 \pm 0.3$ and $-1.3 \pm 0.14$ for And V and And VI, respectively. The larger errors in our And V estimates are due to the lower resolution of our LRIS data and the fact that we exclude the third line of the triplet from our calculation of [Fe/H] as it has been artificially broadened by skylines.

$M_V \leq -7.9$ rather than $M_V \leq -8$ as it allows us to include the MW object Canes Venatici I (CVnI) in our sample. This object has more in common with the classical MW dSph than the ultrafaint population, and it is quite similar to a number of the classical M31 dSph in terms of its luminous component, with a larger $r_{half}$ for its luminosity than typical MW objects. Therefore it is interesting to examine how it compares with both populations.

With the sample defined, we now investigate the claims of Walker et al. (2009) that the MW dSph are consistent with being born in a Universal dark matter halo, i.e. a halo where the mass contained within a given radius is identical for all dSph, irrespective of their luminosity. We plot $r_{half}$ versus $\sigma_v$, for our sample, adding our newly derived velocity dispersions for And V and And VI in Fig. 8, where the MW dSph are plotted as red triangles, and the M31 objects as blue circles. Here we overlay the best-fitting Cored and Navarro–Frenk–White (NFW) mass profiles from Walker et al. (2009), which were derived using the $\sigma_v$ and $r_{half}$ data from MW satellites. Our MW data come from Walker et al. (2009), and references within, with an updated value for the velocity dispersion of Boötes from (Koposov et al. 2011). Our M31 data have been taken from Letarte et al. (2009), Collins et al. (2010), Kalirai et al. (2010) and references therein. Our two new measurements for And V and And VI agree well with the Walker et al. (2009) relations, as do And I, And VII and And XV, demonstrating that while M31 does appear to have a population of colder outliers, among its brighter population there is a significant fraction of dSph that agree well with their MW counterparts. This raises the question, what is the difference between these systems and their colder brethren?

Whilst the M31 dSph scatter towards colder velocity dispersion for a given size, the MW dSph scatter in the opposite direction, with four of the nine (Dra, Scl, UMi and For) satellites lying over $1\sigma$ from the NFW and Core profiles in the hotter sense, while only one member of this population (CVnI) falls below it. Even as we go to lower luminosities, shown as small green points, we find only one other dSph that is colder than these relations, the Hercules dSph, which several authors (e.g. Sand et al. 2009; Jin & Martin 2010) claimed may not be a dSph at all, but a stellar stream of debris formed from the disruption of a dwarf satellite. Similarly, while five of our 10 M31 objects are significantly colder than these relations, only one of these objects

(And I) appears to be significantly hotter than predicted. We show the two isolated Local Group dSph, Cetus (Cet) and Tucana (Tuc) in Fig. 8, and these are also seen to be outliers to the MW relations, with hotter dispersions than expected from the best-fitting profiles.

To see how significant these deviations are, we measure the statistical offset of the 'classical' dSph of both the MW and M31 from these profiles. To do this, we calculate the difference between the velocity dispersion of each object, and the expected velocity dispersion given by the best-fitting NFW and Core profiles for a dSph of the same half-light radius, and we divide this by the $1\sigma$ errors associated with the object in question. This will allow us to measure the scatter for both populations, as well as the average offset, $\langle|\sigma|\rangle$. Taking the MW sample first, we measure an average deviation of $\langle|\sigma_{MW,NFW}|\rangle = 1.64$ and $\langle|\sigma_{MW,Core}|\rangle = 1.44$. If these profiles were truly a good fit for this population, one would expect to see a scatter of order $\langle|\sigma|\rangle \approx 0.2$–0.3. This implies that the MW dSph in our sample are not well fitted by these mass profiles. In fact, if we look at the distribution of the scatter, we find that five out of nine, or 55 per cent, of the dSph in this sample are distinct from these profiles beyond their $1\sigma$ errors. Further, we note that two of the MW dSph, For and CVnI, are outliers at $>3\sigma$ for both profiles. If these profiles were truly Universal, one would not expect to see two such significant outliers from a population of nine objects (i.e. 22 per cent). We also perform this exercise in a sign-dependent fashion to see if there is a preferred direction for the scatter in the MW dSph about these profiles. Here we find $\langle\sigma_{MW,NFW}\rangle = +0.72 \pm 0.2$ and $\langle\sigma_{MW,Core}\rangle = +0.5 \pm 0.1$, where the errors represent the standard deviation of these measurements. This suggests that the MW sample scatter more in the positive or 'hotter' direction about these best-fitting profiles. Performing the same analysis with the M31 'classical' dSph, we find $\langle|\sigma_{MW,NFW}|\rangle = 1.52$ and $\langle|\sigma_{MW,Core}|\rangle = 1.4$. This shows that the scatters about these profiles for the MW and M31 dSph are very similar, and that the profiles of Walker et al. (2009) are not a demonstrably worse fit to these objects. The typical errors on the M31 velocity dispersions are larger than their MW counterparts, and as these are reduced in size with future observations, we will see if this fit gets better or worse. Again, we note that there are two significant outliers in the M31 system, And II and And X, both of which sit more than $3\sigma$ below the best-fitting relations, and that six of the 10 M31 dSph (60 per cent) are outliers to the
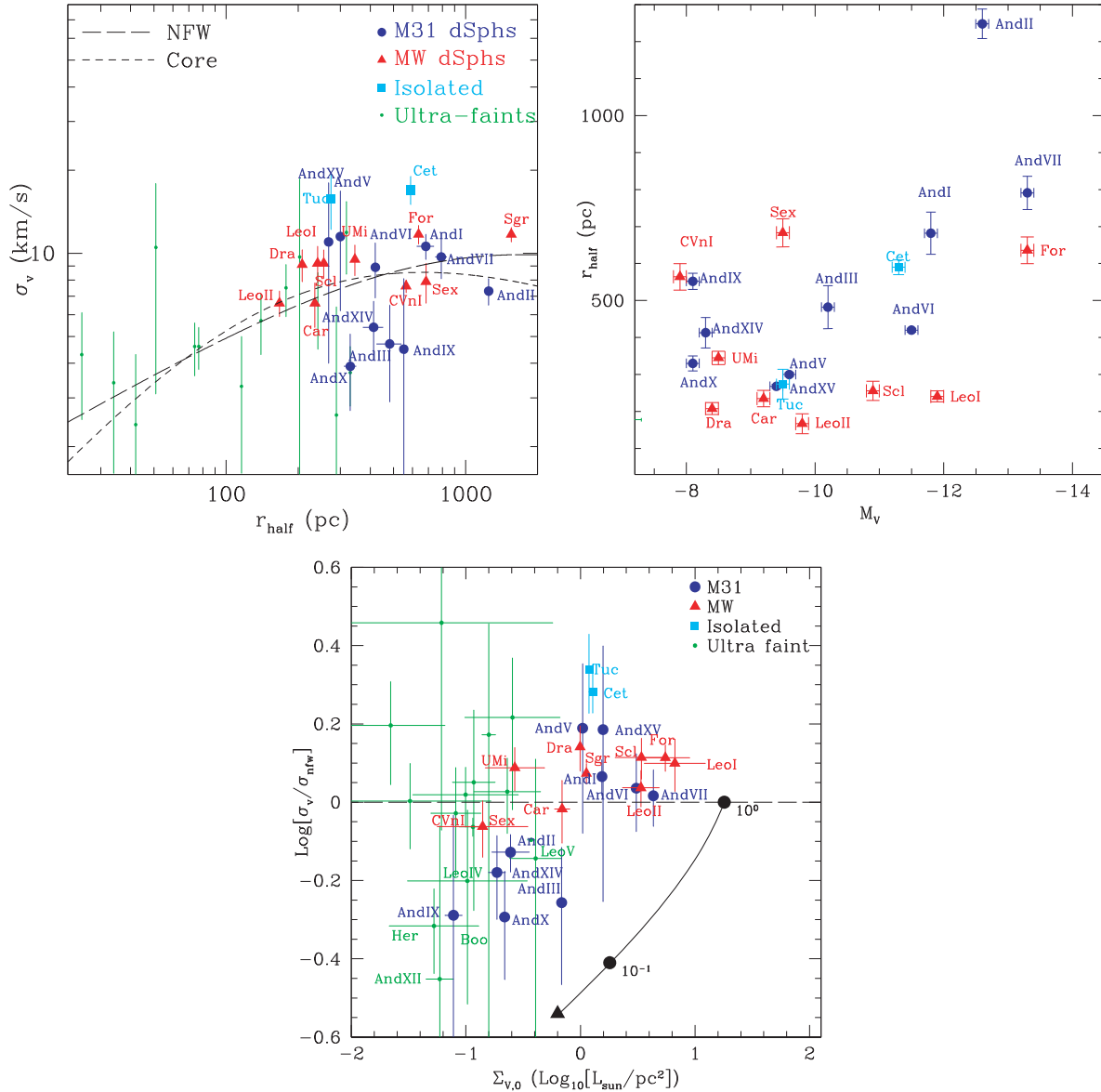
**Figure 8.** Left: $r_{half}$ versus $\sigma$ for the M31 (blue circles), MW (red triangles) and isolated (cyan squares) 'classical' dSph. M31 dSph tend towards colder values than the best-fitting MW relations (NFW, Cored and power law shown as long-dash, short-dash and solid lines) taken from Walker et al. (2009); it was observed in ~50 per cent of this sample. The 'classical' MW dSph have a tendency to scatter above this relation (with the notable exception of CVnI). The two isolated dSph, Cetus and Tucana are significantly hotter than the MW mass profiles. We also show the MW and M31 ultrafaint objects (i.e. $M_V > -7.9$) as small green points. The majority of these are consistent with the relations, barring And XII and Hercules which are both colder. Right: $M_V$ versus $r_{half}$ for the 'classical' population, colour-coded as before. A number of the M31 dSph are more extended for a given luminosity than their MW counterparts. Interestingly, a number of the more extended M31 objects also fall within the colder regime of the previous plot. Lower: central surface brightness ($\Sigma_{V,0}$) versus scatter for all dwarfs about the best-fitting NFW profile from the left-hand panel, where the scatter is measured as the difference between the observed velocity dispersion from the observed velocity dispersion, divided by the expected dispersion in the NFW model, $\sigma_v/\sigma_{nfw}$. If these dSph all inhabited a 'Universal' halo, you would expect to see the points scattering around zero, but instead we see a trend of increasingly negative scatter with decreasing central surface brightness. We overplot the expected path for an object undergoing tidal disruption to follow in this plane, from Peñarrubia, McConnachie & Navarro (2008). The black points represent a dwarf which has yet to lose any mass from tides, and the point at which it has lost 9/10th of its mass. It follows our observed trend well, and we argue that tides have likely played some part in the scatter about a 'Universal' mass profile.

relation at $>1\sigma$. Again, assessing the scatter of the population in a sign-dependent manner, we find $\langle\sigma_{M31,NFW}\rangle = -0.80 \pm 0.2$ and $\langle\sigma_{M31,Core}\rangle = -0.59 \pm 0.4$, showing that these objects preferentially scatter in the more negative or 'colder' direction. Overall, we find that the distribution about these profiles (for both M31 and MW) demonstrates that there is more scatter overall than you would expect solely from their individual errors, as only eight out of 19 (or 42 per cent) objects sit within $1\sigma$ of their expected values. Finally, we

note that the two isolated dSph, Cetus and Tucana, are significant ($>4\sigma$ for Cetus and $>2\sigma$ for Tucana) outliers to the relations.

This spread in the overall population (MW, M31 and isolated dSph combined) suggests that some physical factor is driving the scatter about these relations, and we argue that tidal forces exerted by the host could play a part in creating the observed differences in both the central velocity dispersions and surface brightnesses between MW and M31 satellites. The work of Peñarrubia et al.

(2010) explored the masses and kinematics of the dSph populations for two host galaxies with the same total mass, but with stellar discs whose masses differed by a factor of 2. They found that the dSph orbiting the heavier disc had lower masses and intrinsic velocity dispersions for a given half-light radius than those in the lower disc-mass system, and that these differences were caused by tidal forces exerted from this more massive central disc. This mechanism was also discussed in Walker et al. (2010) as a possible explanation of the discrepancy between the M31 dSph and the McGaugh et al. (2007) mean rotation curve. We know from various studies (e.g. Hammer et al. 2007) that the stellar disc of M31 is roughly twice as massive as the MW disc, and we do indeed see colder dispersions for a given half-light radius in M31, cf. MW. It is thus plausible that this larger disc-to-halo mass ratio has influenced the kinematic properties for a number of M31 dSph. Those that seem more typical in terms of their velocity dispersions and central masses could then either be on orbits about their host that cause them to feel the tidal forces of the disc less keenly than their counterparts, such as And V and And VI, or could have been accreted to M31 at a later time. The tendency for the MW objects to spread in the opposite direction could also be explained using similar arguments. Tides may have played a more significant role in the evolution of the colder CVnI, the only classical MW that falls significantly below the Walker 2009 relations. While no extreme extratidal population has been reported for this object, it is quite extended along its major axis (an extension of ∼2 kpc, Martin et al. 2008).

Another discrepancy between brighter MW and M31 dSph is that the latter have a tendency to be more extended for a given luminosity than their MW counterparts (McConnachie & Irwin 2006a). In the right-hand panel of Fig. 8, we plot the absolute magnitudes of both the 'classical' M31 and MW dSph as a function of their half-light radius. Interestingly, a number of the more extended M31 objects in this panel also fall within the colder regime of the previous plot, meaning the colder objects tend to have larger scale-radii than those that are observed to be more typical or hotter. In the lower panel of Fig. 8 we demonstrate this trend by plotting the logarithm of central surface brightness, $\log[\Sigma_{V,0}]$ (where we measure $\Sigma_{V,0} = L_{\text{half}}/\pi r_{\text{half}}^2$) against the logarithm of the scatter about the best-fitting NFW profile in the $\sigma_{\text{v}}-r_{\text{half}}$ plane, where the scatter is measured as the ratio of the observed velocity dispersion to the expected dispersion in the NFW model, $\log[\sigma_{\text{v}}/\sigma_{\text{nfw}}]$. If these dSph all inhabited a Universal halo, you would expect to see the points scattering around zero, but instead we see a trend of increasingly negative scatter with decreasing central surface brightness. We argue that this is likely driven in part by tidal forces. As the dark matter haloes are gradually stripped of mass, they become less dense, causing a drop in their velocity dispersions. At the same time, the stellar surface density decreases as stars are gradually removed. To illustrate the expected path taken by dSph undergoing tidal disruption in this parameter space, we overplot the tidal tracks generated from equation (7) and table 2 of Peñarrubia et al. (2008) and note that it follows the same direction as our data, indicating that tides have likely played some part in the evolution of these objects away from their initial mass profiles. The black points represent a dwarf that has yet to lose any mass from tides, and the point at which it has lost 9/10th of its mass. This figure clearly demonstrates that for some of the highest surface brightness MW objects (e.g. Leo I, Scl and For), the NFW profile from Walker et al. (2009) agrees poorly with the observed dispersions for these objects, underestimating them by ∼0.1 dex. These objects would have their central dispersions and masses modelled better with halo profiles that possessed a higher circular velocity than that used by Walker et al. (2009) ($V_c$

∼ 18 km s$^{-1}$, cf. $V_c$ ∼ 15 km s$^{-1}$), although such a profile would be demonstrably worse for the colder MW and M31 objects. This finding strongly argues against the notion that all dSph currently reside in a Universal halo. We also plot the positions of the ultrafaint dSph in this plane; however, owing to the large uncertainties in measured values of luminosity, half-light radius and velocity dispersion, they demonstrate a large scatter about the expected value of zero. We note that there are a number of ultrafaints that have significantly colder dispersions than expected for their surface brightness, including Hercules, Boötes and And XII, suggesting that tides likely play an important role in shaping these objects.

Exploring this tidal origin as an explanation for these differences, we turn to the kinematic properties of the two isolated Local Group dSph, Cetus and Tucana. Owing to their large distances from either MW or M31 (755 and 890 kpc), they are not thought to have felt a strong tidal force from either galaxy over the course of their evolution. For the Cetus dSph, analyses of both INT photometry and Keck DEIMOS spectroscopy (McConnachie & Irwin 2006a; Lewis et al. 2007) have shown no evidence for previous or ongoing tidal disruption, and its large tidal radius (6.6 kpc, McConnachie & Irwin 2006a) implies that tidal forces from either MW or M31 are unlikely to have played a significant role in its evolution. Similarly, Tucana shows no obvious signs of tidal disruption, other than an absence of H I gas (Fraternali et al. 2009) which could have been expelled by stellar feedback, or tidally removed. As it has an unusually large receding velocity with respect to MW ($v_{\text{r}} = +98.9$ km s$^{-1}$, Fraternali et al. 2009), it has been argued that Tucana may be on a highly elongated orbit about MW, bringing it in close proximity to our Galaxy ∼10 Gyr ago, meaning it may have experienced stronger tidal forces than Cetus. Given its current position, it is unlikely to have completed more than one orbit within the Local Group, and therefore has experienced less tidal-stirring over the course of its history compared with the M31 and MW dSph. In our analysis here, we find that both these objects are positioned in the hotter $r_{\text{half}}-\sigma_{\text{v}}$ regime, with Cetus being a more extreme outlier than Tucana. This fits with our expectation if tidal forces from the host are the cause of this scatter about a Universal profile.

These results demonstrate that, while other factors may also be involved in shaping the physical and dynamical properties of the dark matter haloes of dSph, the effects of tidal forces exerted by the host galaxy play an important role in setting the underlying mass profiles of its associated satellite population. In the context of the MW and M31 systems, we argue that the observed scatter towards colder velocity dispersions in the M31 subhaloes is likely due to the larger disc-to-halo mass ratio in this system compared with MW.

## 5 CONCLUSIONS

In this study, we set out to further investigate the results of Collins et al. (2010) and Kalirai et al. (2010) who noted that the velocity dispersions and central masses of a number of the M31 dSph differed significantly from MW dSph of similar scale-radii, making them outliers to the universal mass profiles derived for the MW dSph, and the McGaugh et al. (2007) mean rotation curve (Walker et al. 2009, 2010). We restricted ourselves to studying the 'classical' dSph in both galaxies, where classical was defined as any dSph with $M_V$ < −7.9 to avoid complications introduced by the uncertain nature of some ultrafaint dwarfs, and low-number statistics for the faint M31 dSph. We have also presented updated structural properties and kinematic properties for two of the classical M31 population, And V and And VI, for whom only systemic velocities have previously been reported (Guhathakurta et al. 2000). We updated values for

their half-light and tidal radii to $r_{half} = 292 \pm 22$ and $440 \pm 16$ pc, $r_t = 1.2 \pm 0.2$ and $1.6 \pm 0.2$ kpc, their PA ($\theta = 32° \pm 2°$ and $\theta = 164° \pm 2°$) and ellipticities ($\epsilon = 0.17 \pm 0.02$ and $0.39 \pm 0.02$) for And V and And VI, respectively. In terms of their kinematics, we measured systemic velocities of $v_r = -393.1 \pm 4.2$ and $-344.8 \pm 2.5$ km s$^{-1}$, and dispersions of $\sigma_v = 11.5^{+5.3}_{-4.4}$ and $9.4^{+3.2}_{-2.4}$ km s$^{-1}$ for And V and And VI, respectively, meaning that these two dSph appear very typical of objects of their size when compared with MW dSph. This result shows that not all of the M31 dSph reside in significantly different dark matter haloes to those of MW. When assessing the classical MW and M31 in the $r_{half}-\sigma_v$ plane, we find that with respect to the best-fitting mass profiles of Walker et al. (2009), scatter about these is observed in both the positive and negative directions, and is greater than would be expected of the measurement errors alone. The scatter in the positive or 'hotter' direction occurs predominantly within the MW population with only one M31 object (And I) found to scatter in this direction, and similarly, all but one of the 'colder' objects are M31 dSph (the exception being CVnI). We also find a tendency for the 'hotter' dSph to be more compact for a given luminosity than the 'colder' objects. This is seen when comparing the central surface brightnesses of these objects with deviations of their velocity dispersions from the best-fitting Walker et al. (2009) NFW profile. In this plane, we can clearly see that deviations towards colder velocity dispersions increase as surface brightness decreases. Analysing this in the framework of Peñarrubia et al. (2010) where the colder velocity dispersions of the M31 dSph are suggested to be the result of a more massive disc-to-halo mass ratio in M31 compared to MW, we argue that the underlying mass profiles for dwarf galaxies are not Universal, and are influenced by the baryonic component of disc galaxies, causing variation from host to host.

## ACKNOWLEDGMENTS

## REFERENCES

Armandroff T. E., Davies J. E., Jacoby G. H., 1998, AJ, 116, 2287
Armandroff T. E., Jacoby G. H., Davies J. E., 1999, AJ, 118, 1220
Battaglia G., Irwin M., Tolstoy E., Hill V., Helmi A., Letarte B., Jablonka P., 2008, MNRAS, 383, 183
Belokurov V. et al., 2006, ApJ, 647, L111
Belokurov V. et al., 2007, ApJ, 654, 897
Belokurov V. et al., 2008, ApJ, 686, L83
Chapman S. C., Ibata R., Lewis G. F., Ferguson A. M. N., Irwin M., McConnachie A., Tanvir N., 2006, ApJ, 653, 255
Chapman S. C. et al., 2007, ApJ, 662, L79
Collins M. L. M. et al., 2010, MNRAS, 407, 2411
Dotter A., Chaboyer B., Jevremović D., Kostov V., Baron E., Ferguson J. W., 2008, ApJS, 178, 89
Fraternali F., Tolstoy E., Irwin M. J., Cole A. A., 2009, A&A, 499, 121
Guhathakurta P., Reitzel D. B., Grebel E. K., 2000, in Bergeron J., ed., SPIE Conf. Ser. Vol. 4005, Keck Studies of M31's Stellar Halo. SPIE, Bellingham, WA, p. 168
Hammer F., Puech M., Chemin L., Flores H., Lehnert M. D., 2007, ApJ, 662, 322
Harbeck D., Gallagher J. S., Grebel E. K., Koch A., Zucker D. B., 2005, ApJ, 623, 159
Illingworth G., 1976, ApJ, 204, 73
Irwin M., Lewis J., 2001, New Astron. Rev., 45, 105
Jin S., Martin N. F., 2010, preprint (arXiv: 1010.2389)
Kalirai J. S. et al., 2010, ApJ, 711, 671
Kirby E. N., Simon J. D., Geha M., Guhathakurta P., Frebel A., 2008, ApJ, 685, L43
Kirby E. N., Lanfranchi G. A., Simon J. D., Cohen J. G., Guhathakurta P., 2011, ApJ, 727, 78
Koposov S. et al., 2008, ApJ, 686, 279
Koposov S. E. et al., 2011, ApJ, in press, preprint (arXiv:1105.4102)
Letarte B. et al., 2009, MNRAS, 400, 1472
Lewis G. F., Ibata R. A., Chapman S. C., McConnachie A., Irwin M. J., Tolstoy E., Tanvir N. R., 2007, MNRAS, 375, 1364
Martin N. F., Ibata R. A., Chapman S. C., Irwin M., Lewis G. F., 2007, MNRAS, 380, 281
Martin N. F. et al., 2008, ApJ, 672, L13
Mateo M. L., 1998, ARA&A, 36, 435
McConnachie A. W., Côté P., 2010, ApJ, 722, L209
McConnachie A. W., Irwin M. J., 2006a, MNRAS, 365, 1263 (M06a)
McConnachie A. W., Irwin M. J., 2006b, MNRAS, 365, 902
McConnachie A. W., Irwin M. J., Ferguson A. M. N., Ibata R. A., Lewis G. F., Tanvir N., 2005, MNRAS, 356, 979
McConnachie A. W., Arimoto N., Irwin M., 2007, MNRAS, 379, 379
McConnachie A. W. et al., 2009, Nat, 461, 66
McGaugh S. S., de Blok W. J. G., Schombert J. M., Kuzio de Naray R., Kim J. H., 2007, ApJ, 659, 149
Minor Q. E., Martinez G., Bullock J., Kaplinghat M., Trainor R., 2010, ApJ, 721, 1142
Niederste-Ostholt M., Belokurov V., Evans N. W., Gilmore G., Wyse R. F. G., Norris J. E., 2009, MNRAS, 398, 1771
Peñarrubia J., McConnachie A. W., Navarro J. F., 2008, ApJ, 672, 904
Peñarrubia J., Benson A. J., Walker M. G., Gilmore G., McConnachie A. W., Mayer L., 2010, MNRAS, 406, 1290
Richardson J. C. et al., 2011, ApJ, in press, preprint (arXiv: 1102.2902)
Richstone D. O., Tremaine S., 1986, AJ, 92, 72
Sand D. J., Olszewski E. W., Willman B., Zaritsky D., Seth A., Harris J., Piatek S., Saha A., 2009, ApJ, 704, 898
Schlegel D. J., Finkbeiner D. P., Davis M., 1998, ApJ, 500, 525
Simon J. D. et al., 2010, ApJ, submitted, preprint (arXiv: 1007.4198)
Starkenburg E. et al., 2010, A&A, 513, A34
Strigari L. E., Bullock J. S., Kaplinghat M., Simon J. D., Geha M., Willman B., Walker M. G., 2008, Nat, 454, 1096
Tollerud E. J., Bullock J. S., Strigari L. E., Willman B., 2008, ApJ, 688, 277
Walker M. G., Mateo M., Olszewski E. W., Gnedin O. Y., Wang X., Sen B., Woodroofe M., 2007, ApJ, 667, L53
Walker M. G., Mateo M., Olszewski E. W., Peñarrubia J., Wyn Evans N., Gilmore G., 2009, ApJ, 704, 1274
Walker M. G., McGaugh S. S., Mateo M., Olszewski E. W., Kuzio de Naray R., 2010, ApJ, 717, L87
Willman B. et al., 2005a, AJ, 129, 2692
Willman B. et al., 2005b, ApJ, 626, L85
Willman B., Geha M., Strader J., Strigari L. E., Simon J. D., Kirby E., Warres A., 2010, AJ, submitted, preprint (arXiv: 1007.3499)
Wolf J., Martinez G. D., Bullock J. S., Kaplinghat M., Geha M., Muñoz R. R., Simon J. D., Avedo F. F., 2010, MNRAS, 406, 1220
Zucker D. B. et al., 2006a, ApJ, 650, L41
Zucker D. B. et al., 2006b, ApJ, 643, L103

This paper has been typeset from a TeX/LaTeX file prepared by the author.